Wood Science and Technology
https://doi.org/10.1007/s00226-024-01597-4

ORIGINAL

Accuracy of digital image correlation system with telecentric lens for compression tests of wood

Masaki Teranishi[1] · **Doppo Matsubara**[2]

Received: 7 June 2024 / Accepted: 23 August 2024

Abstract

The digital image correlation (DIC) system is a powerful tool for measuring distributions of displacement and strain on the surface of a specimen. DIC systems are employed not only for homogeneous materials such as metals but also for heterogeneous materials such as wood. Although numerous validations of DIC system accuracy for metallic materials exist, the accuracy verification for wood, especially under multiaxial stress conditions, is less common. This study investigated the accuracy of a DIC system equipped with a bilateral telecentric lens on wood (Douglas fir). The accuracy verification in uniaxial stress fields was conducted through full compression testing, while verification in multiaxial stress fields was performed through partial compression testing. Additionally, compression tests on A6063 (aluminium alloy) were conducted to examine the differences in the DIC system accuracy between homogeneous and heterogeneous materials. The accuracy of the DIC system was assessed by comparing the results with those obtained from strain gauges. The results from the full compression tests indicate that the accuracy of axial strain measured by the DIC system was comparable for the specimens of A6063 and Douglas fir in the longitudinal (L) direction but was inferior for Douglas fir in the radial (R) direction. This is because the differences in the mechanical properties of earlywood and latewood produce high strain gradients. Furthermore, the differences in Young's modulus obtained from the DIC system and strain gauge for the specimens of A6063, Douglas fir (L), and Douglas fir (R) were − 1.23%, 2.26%, and − 12.5%, respectively. In the partial compression tests, the accuracy of strain components measured by the DIC system in the specimens of Douglas fir (R) was lower than that in A6063. In the partial compression tests, high strain gradients appear in multiple strain components, leading to a notable decrease in the accuracy of the DIC system compared to the full compression tests.

Extended author information available on the last page of the article

Published online: 31 August 2024

Introduction

The digital image correlation (DIC) system is a noncontact device used to measure displacement and strain on specimens subjected to loading. In contrast to traditional contact extensometers and strain gauges, which measure uniaxial strain at specific points, the DIC system can assess multiaxial strain distribution across an area. Moreover, it can measure strain in extreme environments, such as high temperatures or around a crack where traditional strain measurement techniques are ineffective. Owing to these capabilities, the DIC system is critical in the fields of engineering and materials science.

Typically, a DIC system employs an industrial camera equipped with either a standard or a telecentric lens. A standard lens offers a wide field of view (FOV) but has a limited depth of field (DOF), leading to potential measurement errors due to out-of-plane deformation of the specimen. Conversely, a telecentric lens, while providing a narrower FOV, offers a greater DOF, thereby enhancing accuracy in situations of out-of-plane deformations (Pan et al. 2013). This study utilises a DIC system with a bilateral telecentric lens.

The application of DIC systems in wood research spans from material-level investigations (Iraola et al. 2021; Jeong et al. 2016; Kumpenza et al. 2018; Matsuda et al. 2019; Matsuda et al. 2017; Totsuka et al. 2022; Xavier et al. 2012) to structural testing at the component level (Bakalarz et al. 2023; Navaratnam et al. 2020; Sirumbal-Zapata et al. 2019; Timbolmas et al. 2022). Within these studies, DIC is employed for a variety of purposes, including exploring damage mechanisms (Matsuda et al. 2018, 2017; Navaratnam et al. 2020), determining mechanical properties such as Young's modulus and Poisson's ratio (Jeong et al. 2016; Kumpenza et al. 2018), and verifying the accuracy of finite-element analysis (FEA) (Sirumbal-Zapata et al. 2019; Timbolmas et al. 2022). Establishing methods to quantitatively evaluate the errors associated with DIC is essential for its effective adaptation to specific investigative needs.

The accuracy of DIC systems has been extensively documented by numerous researchers (Demizu et al. 2012; Li et al. 2018; Pan et al. 2013, 2014). The focus has predominantly been on metallic materials, owing to their macroscopic homogeneity and isotropy. The strain measurement accuracy of DIC systems in metals is investigated by comparing its results with those obtained from strain gauges or FEA results. Furthermore, a method for verifying the accuracy of the DIC system in metals under multi-axial stress fields, in addition to uniaxial stress fields, has also been proposed. Despite the robust validation processes in metals, there is few research on DIC accuracy in wood (Xavier et al. 2012). Xavier et al. (2012) conducted full-field compression tests on wood, comparing the Young's modulus derived from DIC systems with those obtained from strain gauges. However, this examination is limited to the uniaxial stress field in the fibre direction and does not address the accuracy of a DIC system in the direction orthogonal to the fibres, where local deformation occurs due to the differences in the mechanical properties of earlywood and latewood. In addition, to the best of the authors'

knowledge, few studies have explored the accuracy verification of DIC systems in wood under multiaxial stress conditions.

This study aims to investigate the accuracy of a DIC system equipped with a bilateral telecentric lens, specifically on wood. The DIC accuracy verification in uniaxial stress fields was performed using full compression tests in the fibre direction and the direction orthogonal to the fibre. The DIC accuracy verification in multiaxial stress fields was examined through partial compression testing. Additionally, to evaluate the influence of wood's anisotropic and macroscopically heterogeneous nature on DIC accuracy, comparative tests were conducted using A6063 (an aluminium alloy), which is isotropic and homogeneous.

Experiment

Materials and specimens

Douglas fir (*Pseudotsuga menziesii*), imported from Canada, was selected for the test specimens. Because of the imported nature of the wood, it was challenging to ascertain the exact age and region of origin of the tree. Wooden boards were cut from a Douglas fir log, and the bending moduli of these boards were assessed using a grading machine in accordance with the Japan Agricultural Standard 1083 (JAS 2019). The Douglas fir was classified as grade E150, indicating a nominal Young's modulus of 15,000 MPa.

To evaluate the accuracy of a DIC system between the fibre direction and the direction orthogonal to the fibre under a uniaxial stress field, test specimens for uniform compression in longitudinal (L) and radial (R) directions were prepared, as depicted in Fig. 1a and b, respectively. The specimens for full compression tests in the L and R directions of Douglas fir were designated as DF-L-FC and DF-R-FC, respectively. Additionally, two types of partial compression test specimens were prepared, as shown in Fig. 1 (c) and (d); these were named DF-PC-A and DF-PC-B, respectively, with the location of strain gauges on these specimens determined based on strain distribution data from FEA, as detailed in Sect. "FEA of partial compression test". The experimental procedures for both full and partial compression tests adhered to the Japan Industrial Standard (JIS) Z 2101 (JIS 2020). The compressive load was applied by the universal testing machine. The displacement control mode of the universal testing machine was used with constant speed that reached the yield stress within 1–2 min from the start of loading. However, in the compression tests, the imposed displacement was stopped for a few seconds during imaging for DIC, so it was not strictly at a constant displacement speed. Table 1 lists the numbers, densities, and moisture contents of the specimens.

To facilitate the application of the DIC method on the surfaces of test specimens, a speckle pattern was created using the following procedure:

(1) Uniaxial and triaxial strain gauges (KFGS-series, Kyowa, Japan) were attached to the surfaces of the full and partial compression test specimens, respectively.

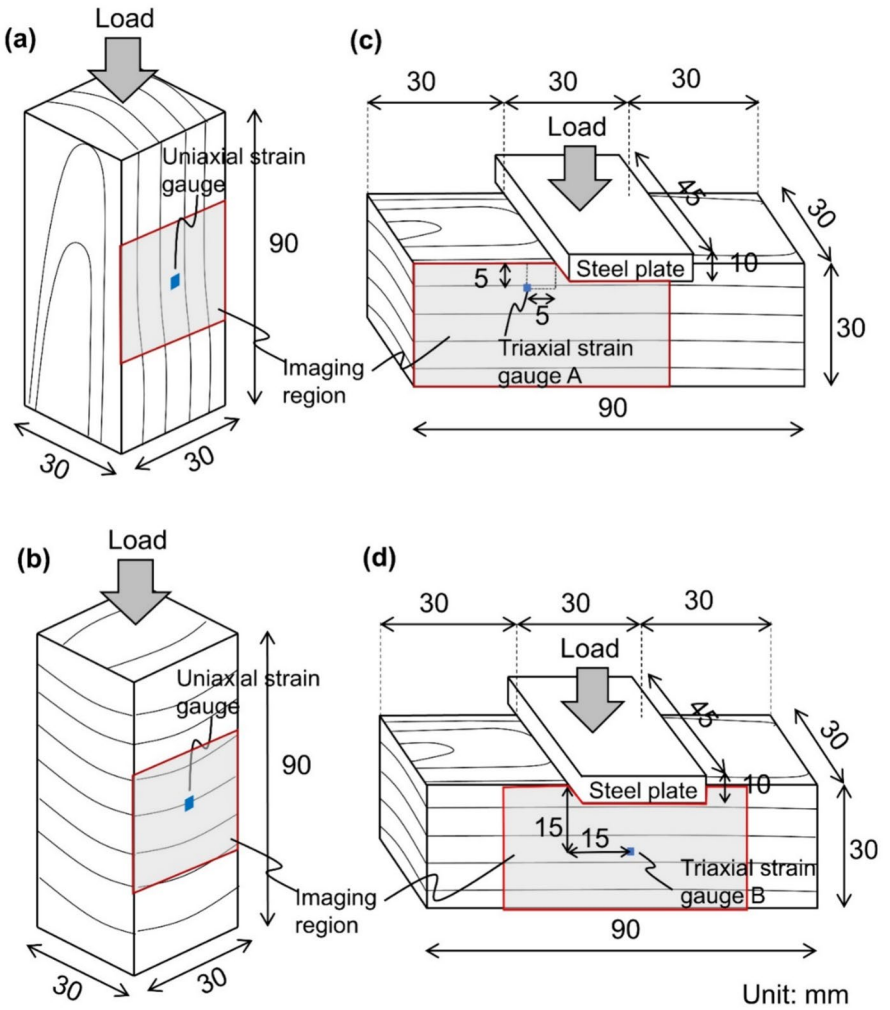

Fig. 1 Dimension, loading schematic, DIC imaging region, and gauge placement and DIC averaging area of interest for specimens **a** DF-L-FC, **b** DF-R-FC, **c** DF-PC-A, and **d** DF-PC-B (colour figure online)

Table 1 Properties of test specimens

Specimen name	Compression	Material	Number	Density (g/cm^3)	Moisture content (%)
DF-L-FC	Full (Fig. 1(a))	Douglas fir	3	0.546 ± 0.015	8.53 ± 0.139
DF-R-FC	Full (Fig. 1(b))	Douglas fir	3	0.514 ± 0.027	8.71 ± 0.094
DF-PC-A	Partial (Fig. 1(c))	Douglas fir	3	0.540 ± 0.042	10.2 ± 0.157
DF-PC-B	Partial (Fig. 1(d))	Douglas fir	3	0.573 ± 0.032	11.1 ± 0.05
AL-FC	Full (Fig. 1(a), (b))	A6063	3	–	–
AL- PC-A	Partial (Fig. 1(c))	A6063	3	–	–
AL- PC-B	Partial (Fig. 1(d))	A6063	3	–	–

(2) The surface of each specimen was coated two or three times with a white lacquer spray (Aspen, Japan) to achieve opacity.
(3) Maintaining a distance of 30 cm from the nozzle, a black lacquer spray (Aspen, Japan) was applied to the surface to form a speckle pattern.

After the tests, the speckle patterns were sanded off, and the moisture content of the specimens was measured using the oven-dry method in accordance with the JIS Z 2101 standard (JIS 2020).

In addition to the tests on wood, full and partial compression test specimens made of an aluminium alloy (A6063) were also prepared with strain gauges and a speckle pattern to compare the accuracy of the DIC method between anisotropic and isotropic materials. The dimensions of the A6063-T5 specimens matched those of the Douglas fir (Fig. 1). These specimens were labelled with the initial 'AL-' in place of 'DF-', as detailed in Table 1.

The quality of speckle pattern was assessed using the mean subset fluctuation S_f (Hua et al. 2011).

$$S_f = \frac{\sum_{P \in F} S_P}{H \times V} \tag{1}$$

where S_P is the subset fluctuation at point P. F is the class of points. $H \times V$ is the size of a speckle pattern. The mean and standard deviation of S_f in all specimens are 173 and 40.6, respectively. Hua et al. (2011) exihibited that a speckle pattern with large S_f produces a small mean bias error. In addition, their results exihibited that the reduction rate of mean bias error associated with the increase in S_f decreases as S_f increases. Since the maximum value of S_f shown in their study is 114, the S_f in this study is sufficiently large. Based on the above, it is assumed that the quality of the speckle pattern in this study is roughly uniform.

DIC system

Figure 2 illustrates the DIC system, comprising a digital camera (EG600-B, Shodensya, Japan; active pixels: 3072×2048, frame rate: 17fps, sensor: 1/1.8''), a bilateral telecentric lens (RT1, Shodensya, Japan; magnification: 0.1×, working distance: 230 mm, telecentric depth: 34.8 mm), and a ring light (LED-120MM, Shodensya, Japan). The size of field of view (FOV) is 63.1 mm×47.3 mm.

During the experiments, the surface images of the test specimens were captured using the DIC system. To compute the displacement and strain distributions from the captured images, an open-source two-dimensional DIC MATLAB program, Ncorr, was utilised (Blaber et al. 2015). The subset radius and subset spacing were configured to 20 pixels and 0, respectively.

If the goal is simply to compare strains measured by strain gauges and DIC systems, 63.1 mm×47.3 mm FOV is unnecessary. It would be better to use a smaller FOV, similar in size to the strain gauges, to enhance the accuracy of the DIC system. However, wood is composed of heterogeneous materials, including earlywood and latewood, which can lead to localized strain concentrations near their interfaces. To

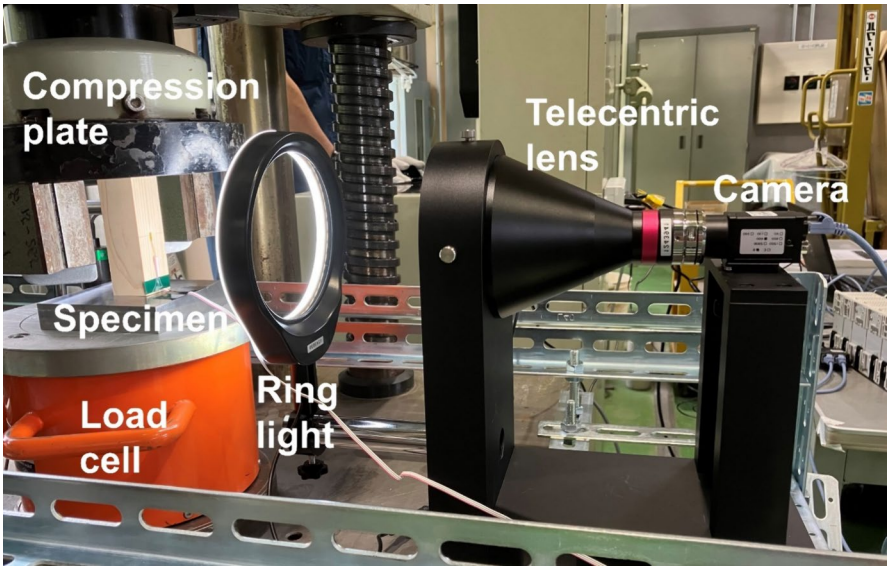

Fig. 2 DIC system

observe the trend of complex strain distributions over most of the specimen's surface, 63.1 mm × 47.3 mm field of view (FOV) was employed. Additionally, considering that many studies (Iraola et al. 2021; Totsuka et al. 2022; Xavier et al. 2012) have reported DIC imaging of large portions of the specimen surface in compression tests similar to those in this research, it is important from a practical perspective to examine the accuracy of such DIC systems. In the case of the partial compression test specimens illustrated in Fig. 1(c) and (d), it is possible to capture two strain gauges within a single image frame. However, these tests were conducted separately for each strain-gauge attachment position to minimise potential errors in strain measurement due to lens distortion in the central imaging area of the DIC system.

Figure 3 shows images of each specimen without a speckle pattern. The *ij* component of strains measured by strain gauges and the DIC system are designated as ε_{ij}^{G} and ε_{ij}^{D}, respectively. The ε_{ij}^{D} values exhibit variability at each point, complicating the direct comparison of ε_{ij}^{G} values from each strain gauge. Therefore, considering the size of the strain gauge in the image, as shown in Fig. 3, the average value of ε_{ij}^{D} (denoted as $\varepsilon_{ij}^{D,ave}$) were computed across a 100-pixel square region centred on the strain gauge part which reads the change in resistance of a material.

FEA of partial compression test

The FEA of the partial compression tests on Douglas fir and A6063 was conducted to determine the strain distribution, which informed the attachment positions of the tri-axial strain gauges. Three-dimensional finite-element models, utilising twenty-node brick elements (C3D20), were developed, replicating the

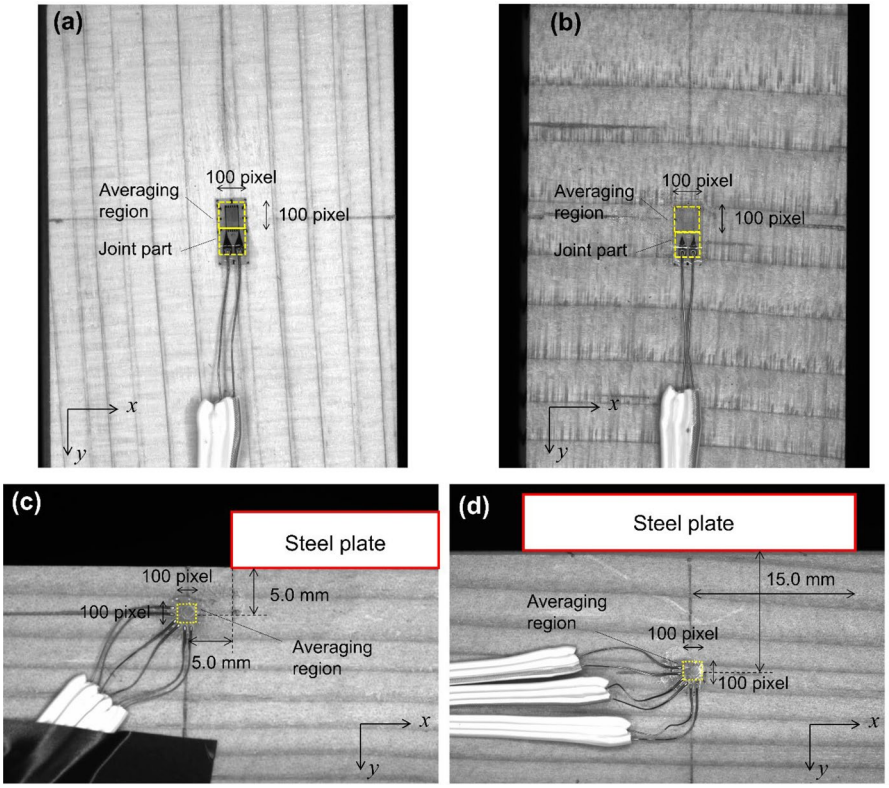

Fig. 3 Images of **a** DF-L-FC, **b** DF-R-FC, **c** DF-PC-A, and **d** DF-PC-B without speckle pattern

dimensions of the partial compression test specimens depicted in Fig. 1(c) and (d). The interface between Douglas fir (or A6063) and steel was modelled using a contact condition with a Lagrange multiplier. A forced displacement of 0.2 mm in the y-direction was applied to the steel plate to simulate a partial compression test on Douglas fir or A6063. In the models, Douglas fir was characterised using Hill's anisotropic yield condition, while A6063 and S45C (steel plate and steel base) were modelled according to the von Mises yield criterion. The mechanical properties of Douglas fir and S45C were sourced from the literature (Teranishi et al. 2024). The Young's modulus, Poisson's ratio, and yield stress for A6063 were determined through uniaxial material testing, with values recorded as 59,462 MPa, 0.34, and 213 MPa, respectively. Figure 4 shows the strain distribution (ε_{xx}, ε_{yy}, and ε_{xy}) for A6063 and Douglas fir. Based on these findings, strain gauge A was positioned beneath the edge of the steel plate, where shear strain is pronounced, whereas strain gauge B was located at the centre of the specimen, where shear strain is minimal and significant compressive strain in the y-direction occurs. Table 2 summarises the signs of each strain component and major strain components for the FEA at strain gauge attachment points A and B.

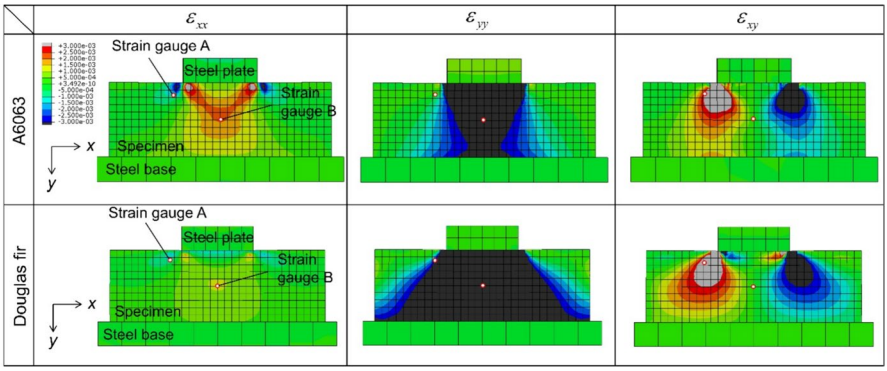

Fig. 4 Strain distributions of A6063 and Douglas fir calculated from FEA

Table 2 Signs of each strain component and major strain components for FEA at strain gauge attachment points

Material	Strain gauge attachment position	ε_{xx}	ε_{yy}	ε_{xy}	Major component
A6063	A	Negative	≈ 0	Positive	ε_{xx}, ε_{xy}
	B	Positive	Negative	≈ 0	ε_{xx}, ε_{yy}
Douglas fir	A	≈ 0	Negative	Positive	ε_{yy}, ε_{xy}
	B	Positive	Negative	≈ 0	ε_{yy}

Results and discussion

Uniaxial material tests

Figure 5 presents representative σ_{yy} versus ε_{yy}^{G} relationships and ε_{yy}^{D} distributions at the initial stage of elastic deformation (2nd step), just before yielding (5th step) and after yielding (6th or 8th step) for AL-FC, DF-L-FC, and DF-R-FC. σ_{yy} is calculated by dividing the compressive force by the entire cross-sectional area of the specimen. In the initial stage (2nd step) of elastic deformation of AL-FC and DF-L-FC, variations in the strain distribution occur owing to partial contact on the top and bottom surfaces caused by geometrical initial imperfections of the test specimen caused by processing. Just before yielding (5th step) of AL-FC and DF-L-FC, the partial contact is relieved, leading to a nearly uniform compressive strain state as compared to initial stage of elastic deformation. However, after yielding of AL-FC and DF-L-FC, bending deformation due to local plastic deformation occurred, reintroducing variability in the strain distribution. Despite AL-FC being a homogeneous material and DF-L-FC being heterogeneous, their tendencies regarding ε_{yy} distribution are similar. The specimens of DF-R-FC exhibited noticeable differences in strain distribution between the earlywood and latewood sections, in contrast to AL-FC and DF-L-FC. Owing to the

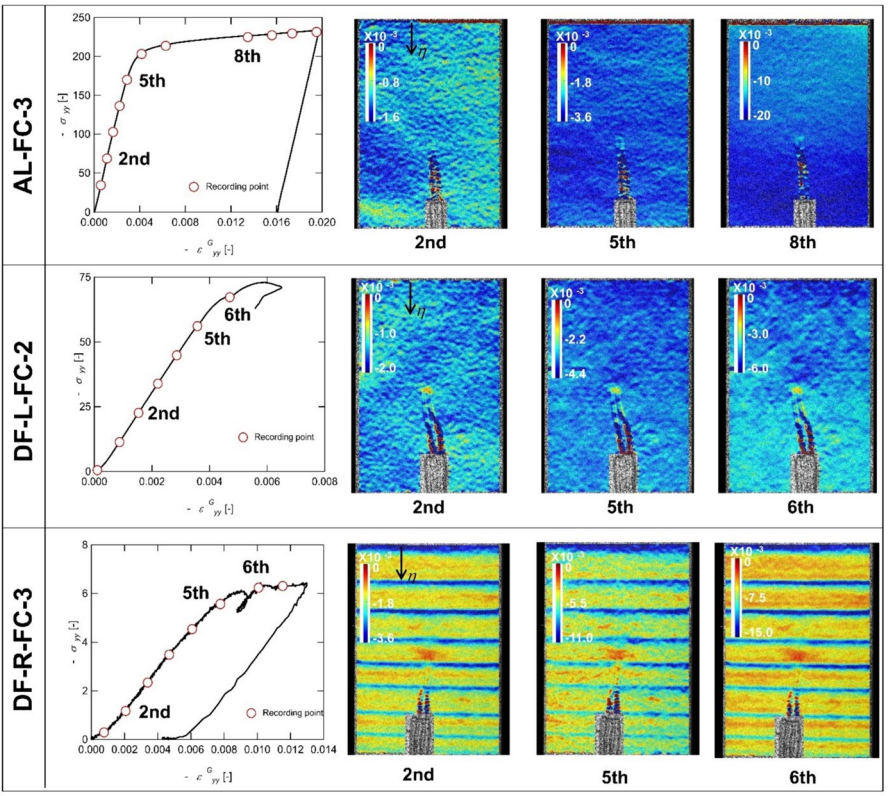

Fig. 5 σ_{yy} versus ε_{yy}^{G} relationships and ε_{yy}^{D} distributions of AL-FC-3, DF-L-FC-2, and DF-R-FC-3

discontinuous change in mechanical properties between earlywood and latewood (Kang et al. 2014), significant compressive strain occurred in the earlywood near the boundary with the latewood. The trend of localised deformation of radial compressive specimens was similar to that reported by Murata et al. (2003).

Figure 6 shows the $\varepsilon_{yy}^{D,ave}$ versus $\left|\varepsilon_{yy}^{G}\right|$ relationships. The maximum values of $\left|\varepsilon_{yy}^{G}\right|$ for AL-FC, DF-L-FC, and DF-R-FC were 0.02, 0.008, and 0.012, respectively,

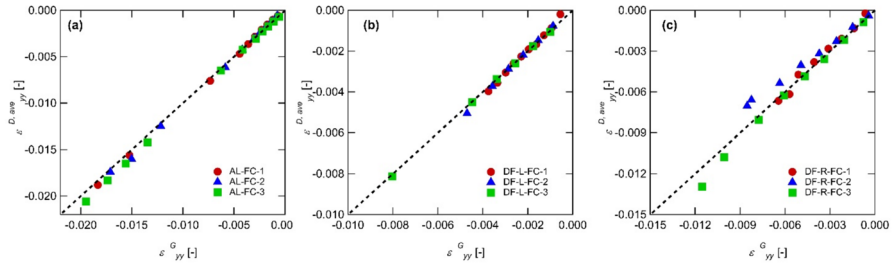

Fig. 6 $\varepsilon_{yy}^{D,ave}$ versus ε_{yy}^{G} relationships of **a** AL-FC, **b** DF-L-FC, and **c** DF-R-FC

with some variability. The cause of this variability is that the specimens of DF-L-FC and DF-R-FC experienced localised deformation in their upper and lower contact regions after yielding, causing fractures such as brooming and crushing, respectively (ASTM 2000).

To evaluate the differences between $\varepsilon_{yy}^{D,ave}$ and ε_{yy}^{G}, the following variables are defined as:

$$\Delta_{ij} = \varepsilon_{ij}^{G} - \varepsilon_{ij}^{D,ave} \tag{2}$$

$$\Delta_{ij}^{rel} = \left(1 - \frac{\varepsilon_{ij}^{D,ave}}{\varepsilon_{ij}^{G}}\right) \times 100 \tag{3}$$

Figure 7 shows the Δ_{yy} versus $\left|\varepsilon_{yy}^{G}\right|$ and Δ_{yy}^{rel} versus $\left|\varepsilon_{yy}^{G}\right|$ relationships. Across all test specimens, there is a tendency for Δ_{yy} to increase as the strain magnitude increases. Notably, the specimens of DF-R-FC exhibit a higher rate of increase in Δ_{yy} compared to those of AL-FC and DF-L-FC. In all specimens, Δ_{yy}^{rel} is substantial ($>10.0\%$) when $\left|\varepsilon_{yy}^{G}\right|$ is small (<0.002), owing to predominant errors of the DIC system such as lens distortion, variations in ambient lighting, self-heating, and temperature variations. When $\left|\varepsilon_{yy}^{G}\right|$ in the specimens of AL-FC and DF-L-FC exceeds 0.002, Δ_{yy}^{rel} stabilises at approximately $\pm$ 6.0% or lower, whereas for DF-R-FC, Δ_{yy}^{rel} continues to increase with $\left|\varepsilon_{yy}^{G}\right|$.

Figure 8 illustrates $\varepsilon_{yy}^{D,ave}$ along the η-axis at the initial stage of elastic deformation, just before yielding and after yielding for (a) AL-FC, (b) DF-L-FC, and (c) DF-R-FC. The η-axis is detailed in the strain distribution diagrams of Fig. 5. There is variability in $\varepsilon_{yy}^{D,ave}$ along the axial distribution in all specimens, which intensifies as axial deformation increases. Specifically, in DF-R-FC-3, this variability is linked to localised strain concentrations at the interface between earlywood and latewood, resulting in higher values of Δ_{yy} and Δ_{yy}^{rel} for DF-R-FC compared to AL-FC and DF-L-FC.

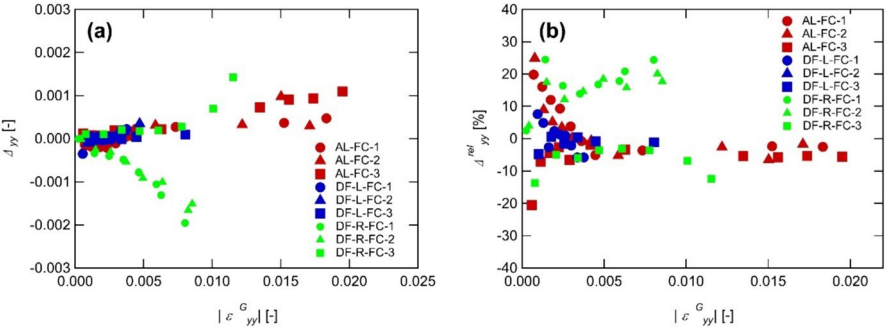

Fig. 7 **a** Δ_{yy} versus $\left|\varepsilon_{yy}^{G}\right|$ and **b** Δ_{yy}^{rel} versus $\left|\varepsilon_{yy}^{G}\right|$ relationships

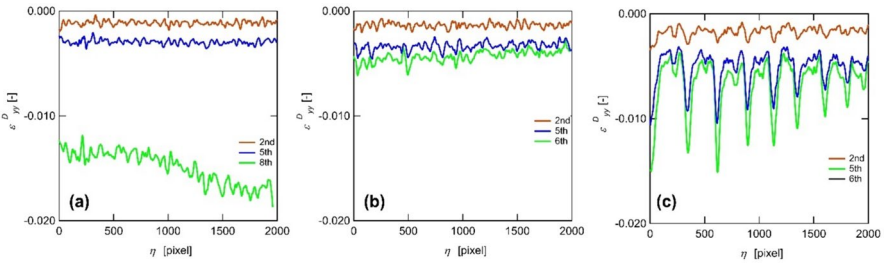

Fig. 8 ε_{yy}^{D} on η-axis for **a** AL-FC-3, **b** DF-L-FC-2, and **c** DF-R-FC-3

It is standard practice to determine the stress–strain relationship of a material in uniaxial material tests using a DIC system to measure the Young's modulus of the material (Chen et al. 2020; Jeong et al. 2016; Pan et al. 2013). Hence, differences in Young's modulus measured by the DIC system and a strain gauge for each specimen are investigated, as listed in Table 3. The average differences in Young's modulus for the specimens AL-FC and DF-L-FC are − 1.23% and 2.26%, respectively, showing nearly similar magnitudes. However, for the specimens of DF-R-FC, the difference is 12.5%, indicating a significantly larger discrepancy compared to the specimens of AL-FC and DF-L-FC. This suggests the importance of recognising the differences in measuring Young's modulus using a DIC system in the radial direction of wood compared to using a uniaxial strain gauge.

Table 3 also indicates a significant discrepancy in the errors of the Young's moduli for DF-R-FC-1 or 2 and DF-R-FC-3. Figure 9 shows the ε_{yy}^{D} distributions of DF-R-FC-2 and DF-R-FC-3, where the averaging region for $\varepsilon_{yy}^{D,ave}$ is indicated. It can be seen that the ε_{yy}^{D} gradient in the averaging region is larger for DF-R-FC-3 compared to DF-R-FC-2. In the DIC system employing the Ncorr program (Blaber et al. 2015), strain components are calculated using numerical differentiation of deformation gradients, which are notably sensitive to noise arising from deformation variations.

Table 3 Young's modulus of each full compression specimen

Specimen	Strain gauge [MPa]	DIC [MPa]	1-DIC/Strain gauge [%]	Average relative difference [%]
AL-FC-1	59,009	61,161	− 3.65	− 1.23
AL-FC-2	57,733	58,717	− 1.70	
AL-FC-3	61,646	60,628	1.65	
DF-L-FC-1	15,318	14,446	5.69	2.26
DF-L-FC-2	15,888	15,677	1.33	
DF-L-FC-3	13,551	13,584	− 0.24	
DF-R-FC-1	1002.9	1171.6	− 16.8	− 12.5
DF-R-FC-2	955.22	1168.9	− 22.4	
DF-R-FC-3	816.81	802.33	1.77	

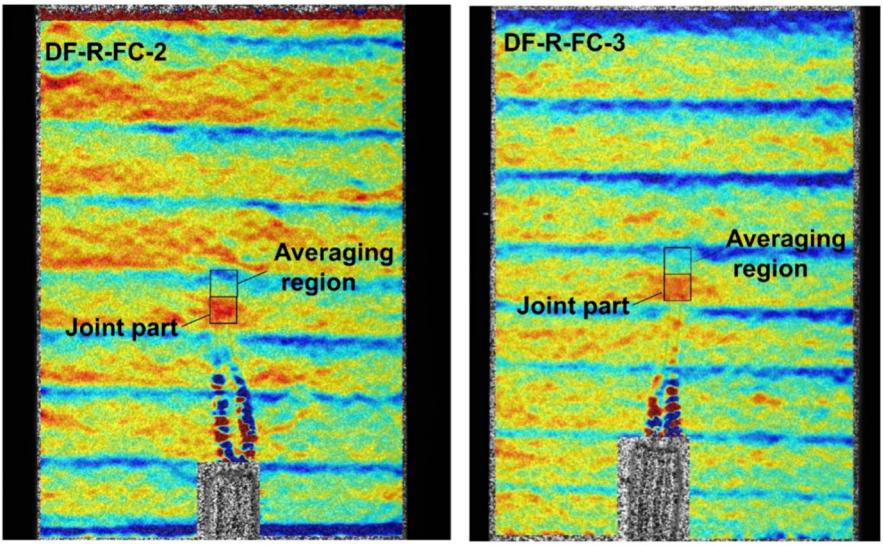

Fig. 9 ε_{yy}^{D} distributions of DF-R-FC-2 and DF-R-FC-3 at 2nd recording point, where the load value is approximately 1.0 kN

The Ncorr program utilises the strain window algorithm (Pan et al. 2009), designed to practically calculate strain distributions. However, in this algorithm, displacement gradients are approximated on a plane to mitigate noise, which may lead to decreased accuracy in the numerical differentiation of strain at points with significant nonlinear displacement gradients. On the other hand, it is known that in regions with high strain gradients, errors from strain gauges can also arise due to averaging effects (Younis et al. 2011). In addition, deriving theoretical formulas from elasticity mechanics for the partial compression problem of wood, which is both orthotropic and heterogeneous, presents significant challenges. Based on the above, in high strain gradient regions, it is necessary to develop methods to accurately evaluate both DIC system and strain gauge. Figures 5 (a), (b), and 9 also show that the lower strain area is the junction of the strain gauge leads because the junction has higher stiffness than the averaged area.

Partial compressive material tests

The partial compressive material tests on A6063 and Douglas fir were conducted. Triaxial strain gauges were affixed to the surfaces of the partial compressive test specimens at two locations, as shown in Fig. 1(c) and (d), and designated as gauges A and B. As illustrated in the top-right corner of Fig. 10, the normal strains measured by these triaxial strain gauges are denoted as ε_0, ε_{45}, and ε_{90}, corresponding to angles of 0°, 45°, and 90° with respect to the x-axis. As shown in Fig. 10, Mohr's strain circle can be illustrated using ε_0, ε_{45}, and ε_{90}, from which the shear strain ε_{xy} can be calculated as follows:

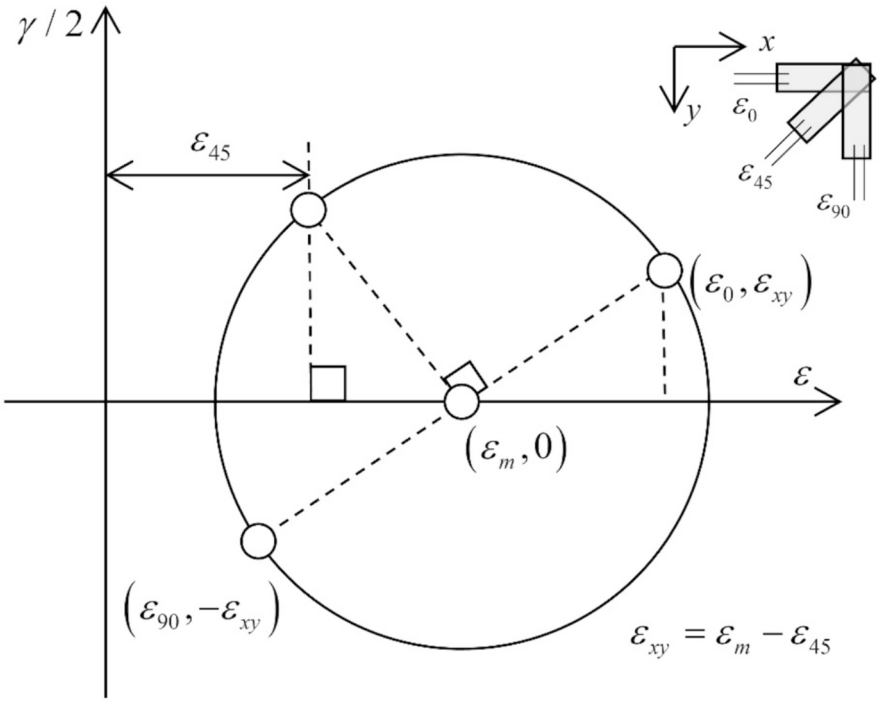

Fig. 10 Mohr's strain circle

$$\varepsilon_{xy} = \varepsilon_m - \varepsilon_{45} = \frac{\varepsilon_0 + \varepsilon_{90}}{2} - \varepsilon_{45} \tag{4}$$

Figures 11 and 12 present the $\varepsilon_{ij}^{D,ave}$ versus ε_{ij}^{G} relationships for the specimens of AL-PC-A, DF-PC-A, AL-PC-B, and DF-PC-B. These results, alongside Table 2, indicate that the signs of each strain component and the major strain components measured from the triaxial strain gauge and DIC correspond with those derived from the FEA results. As ε_{ij}^{G} increases, the difference between $\varepsilon_{ij}^{D,ave}$ and ε_{ij}^{G} in the specimens of AL-PC-A and AL-PC-B increases gradually. Conversely, in the specimens of DF-PC-A and DF-PC-B, the difference increases rapidly beyond a certain value of ε_{ij}^{G}.

Figures 13 and 14 illustrate the Δ_{ij} versus $\left|\varepsilon_{ij}^{G}\right|$ and Δ_{ij}^{rel} versus $\left|\varepsilon_{ij}^{G}\right|$ relationships of PC-A and PC-B, respectively. The observed trends are as follows:

(1) In the specimens of DF-PC-A and DF-PC-B, Δ_{ij} tends to increase with the increase in $\left|\varepsilon_{ij}^{G}\right|$, but it suddenly increases beyond a certain magnitude of $\left|\varepsilon_{ij}^{G}\right|$. In the specimens of AL-PC-A and AL-PC-B, Δ_{ij} tends to increase with the increase in $\left|\varepsilon_{ij}^{G}\right|$, and the values do not exhibit a rapid increase, unlike DF-PC-A and DF-PC-B.

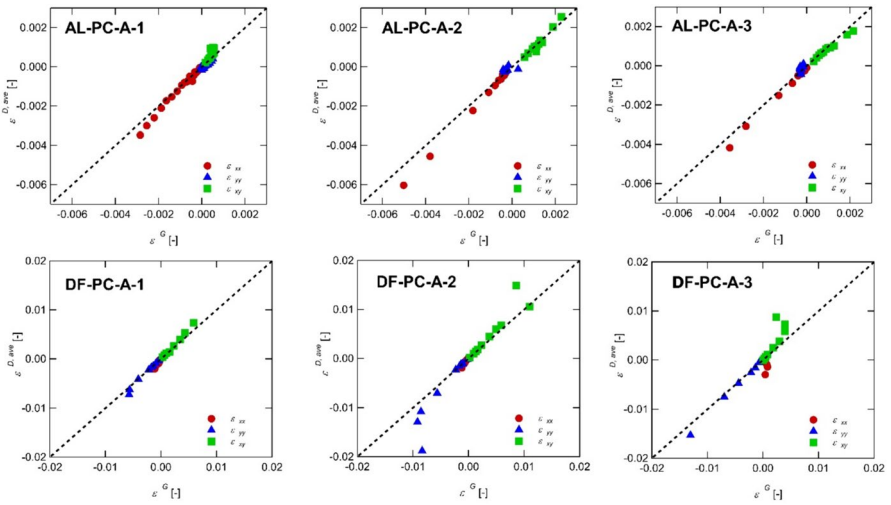

Fig. 11 $\varepsilon_{ij}^{D,ave}$ versus ε_{ij}^{G} relationships of AL-PC-A and DF-PC-A

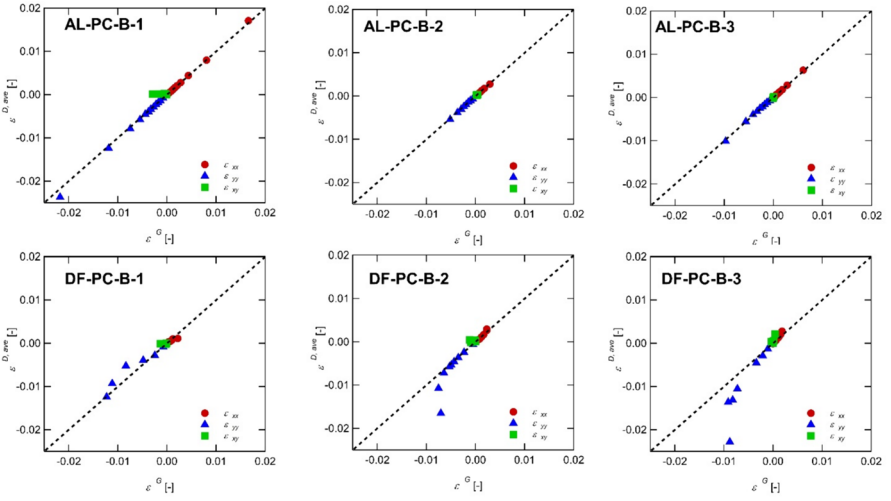

Fig. 12 $\varepsilon_{ij}^{D,ave}$ versus ε_{ij}^{G} relationships of AL-PC-B and DF-PC-B

(2) Within the range of $\left|\varepsilon_{ij}^{G}\right| < 0.002$, Δ_{ij}^{rel} of all the specimens was large (> 20%) owing to unavoidable errors of the DIC system. Within the range of $\left|\varepsilon_{ij}^{G}\right| > 0.002$, Δ_{ij}^{rel} of AL-PC-A and AL-PC-B generally remains within ± 20%, while that of DF-PC-A and DF-PC-B increases with the increase in $\left|\varepsilon_{ij}^{G}\right|$.

(3) In the partial compression tests, Δ_{ij} and Δ_{ij}^{rel} of DF-PC-A and DF-PC-B are larger than those of AL-PC-A and AL-PC-B. Δ_{ij} and Δ_{ij}^{rel} in the partial compression tests are larger than Δ_{yy} and Δ_{yy}^{rel} in the full compression tests.

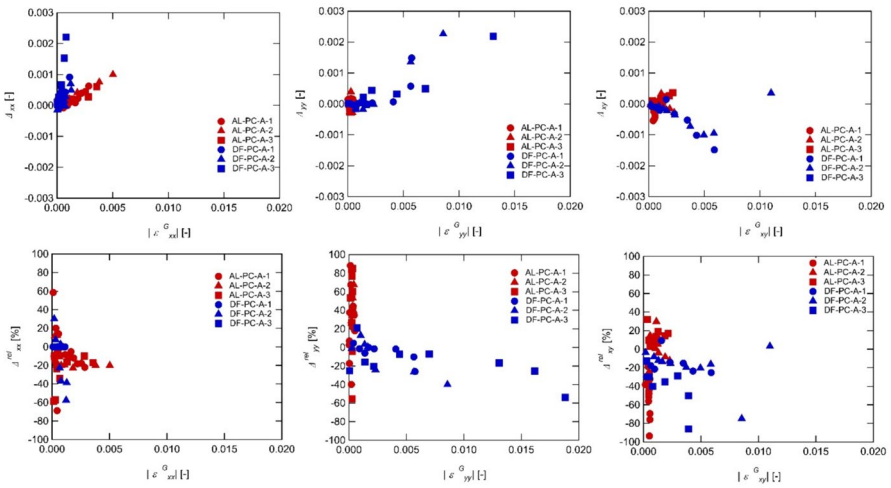

Fig. 13 Δ_{ij} versus $\left|\varepsilon_{ij}^{G}\right|$ and Δ_{ij}^{rel} versus $\left|\varepsilon_{ij}^{G}\right|$ relationships of AL-PC-A and DF-PC-A

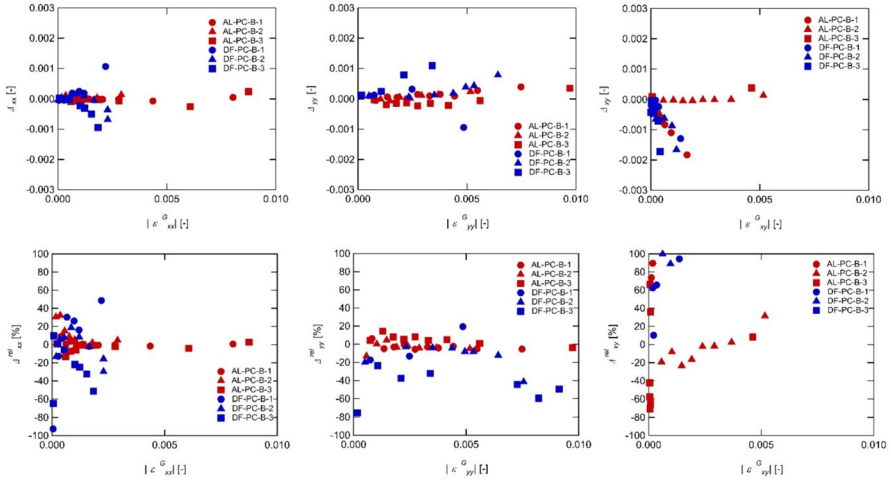

Fig. 14 Δ_{ij} versus $\left|\varepsilon_{ij}^{G}\right|$ and Δ_{ij}^{rel} versus $\left|\varepsilon_{ij}^{G}\right|$ relationships of AL-PC-B and DF-PC-B

To investigate the cause of the rapid increase in Δ_{ij}, as noted in (2), the details of DF-PC-B-3 were examined. Figure 15 shows the P versus u and Δ_{ij} versus u relationships of DF-PC-B-3. The results indicate that Δ_{ij} increases when the P–u relationship exhibits nonlinear behaviour from the 4th to the 7th recording points. At the 7th recording point, Δ_{ij} increases sharply owing to delamination of the speckle pattern near the strain gauge. Figure 16 shows the surface images and distributions of ε_{xx}^{D}, ε_{yy}^{D}, and ε_{xy}^{D} of DF-PC-B-3 at the 4th, 5th, and 6th recording

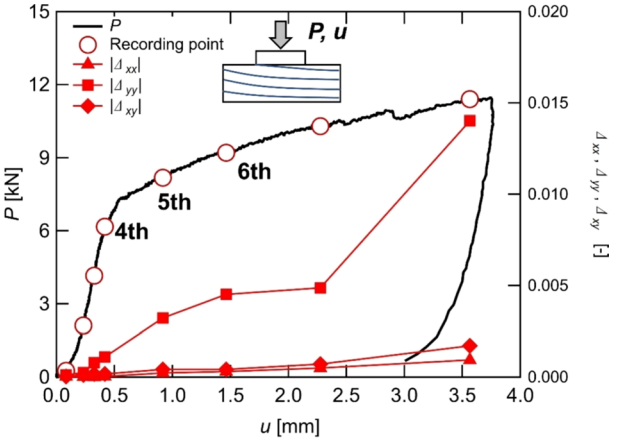

Fig. 15 P versus u and $\left|\Delta_{ij}\right|$ versus u relationships of DF-PC-B-3

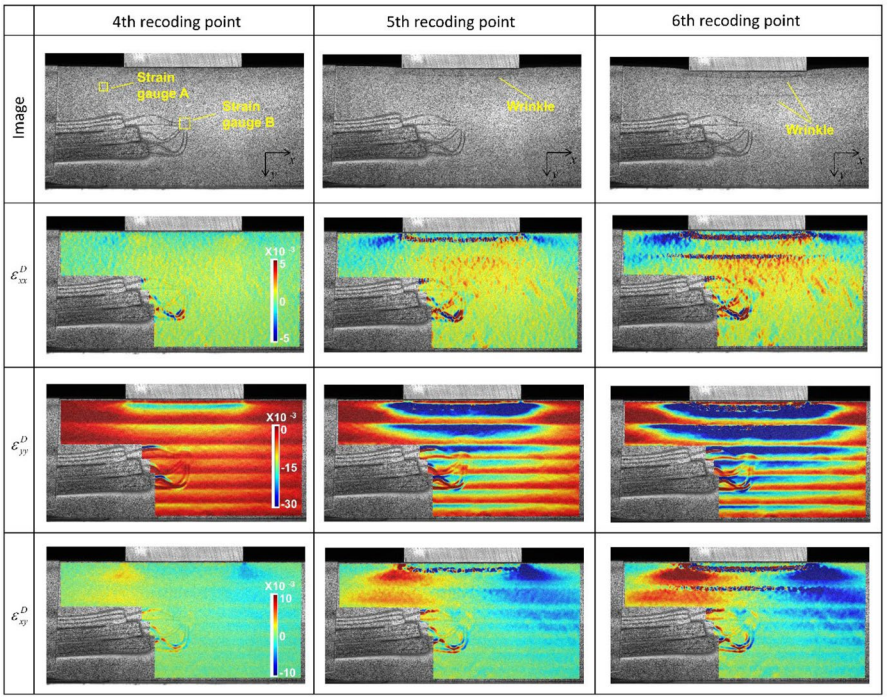

Fig. 16 Images and distributions of ε_{xx}^{D}, ε_{yy}^{D}, and ε_{xy}^{D} of DF-PC-B-3

points. The images show that as the plastic deformation of wood underneath the steel plate progresses, wrinkles form on the surface because of the local deformation of earlywood. The distributions of ε_{yy}^{D} and ε_{xy}^{D} are discontinuous owing to differences in mechanical properties between the earlywood and latewood (Kang

et al. 2014). The discontinuity in the ε_{yy}^{D} distribution extends over a wide range from the top to the bottom of the specimen. In contrast, discontinuities in the distribution of ε_{xy}^{D} are observed from beneath the corner of the steel plate and in the vicinity of the wrinkled portion of the speckle pattern. The discontinuity in ε_{xy}^{D} and ε_{yy}^{D} is mainly observed at the location of strain gauge A, while that in ε_{yy}^{D} is dominant at the location of strain gauge B.

Conclusion

This study investigated the accuracy of a DIC system equipped with a bilateral telecentric lens when applied to wood. Full compression tests and partial compression tests were conducted on Douglas fir and A6063 (aluminium alloy) to examine the differences in the accuracy of the DIC system between homogeneous and heterogeneous materials. The accuracy of the DIC system was assessed by comparing the results with those obtained from strain gauges. In the full compression tests, the accuracy of axial strain measured by the DIC system was similar for the specimens of A6063 and Douglas fir (L: Longitudinal), but the specimens of Douglas fir (R: Radial) exhibited lower accuracy compared to both A6063 and Douglas fir (L). This is because the specimens of Douglas fir (R) exhibited the discontinuous distribution of normal strain in compressive direction owing to differences in mechanical properties between the earlywood and latewood produces high strain gradients.

The differences in Young's modulus obtained from the DIC system and strain gauge for the specimens of A6063, Douglas fir (L), and Douglas fir (R) were -1.23%, 2.26%, and -12.5%, respectively. In the partial compression tests, the accuracy of strain components measured by the DIC system in the specimens of Douglas fir was lower than that in A6063, because of high strain gradients. In partial compression tests, unlike full compression tests, the distribution of multiple strain components exhibits discontinuities and high strain gradients, leading to reduced accuracy of DIC. On the other hand, it is known that in regions with high strain gradients, errors from strain gauges can also arise due to averaging effects. The estimation of errors on orthotropic and heterogeneous materials is challenging. Therefore, in high strain gradient regions, it is necessary to develop methods to accurately evaluate the errors of both DIC system and strain gauge.

Acknowledgements We thank Mr. Yuki Yamagishi and Aruha Terui, graduate students at Niigata University, for their assistance in the experiments.

Author contributions M. T. conducted experiments, analyze the results, wrote the main manuscript text, and prepared all figures and tables. D. M. analyze the results and wrote the part of manuscript text. All authors reviewed the manuscript.

Data availability No datasets were generated or analysed during the current study.

Declarations

Conflict of interest The authors declare no competing interests.

References

Akira D, Hiroshi M, Sho H, Masatoshi M, Masakazu U, Yukihiro I, Chihiro M (2012) fundamental study on improvement in strain measurement accuracy of digital image correlation method. J Japan Soc Civil Eng 68(2):I_683-I_690. https://doi.org/10.2208/jscejam.68.I_683

ASTM (2000) Standard Test Methods for Small Clear Specimens of Timber. ASTM

Bakalarz MM, Tworzewski PP (2023) Application of digital image correlation to evaluate strain, stiffness and ductility of full-scale Lvl beams strengthened by Cfrp. Materials 16(3):1309. https://doi.org/10.3390/ma16031309

Blaber J, Adair B, Antoniou A (2015) Ncorr: open-source 2d digital image correlation matlab software. Exp Mech 55(6):1105–1122. https://doi.org/10.1007/s11340-015-0009-1

Chen B, Chen W, Pan B (2020) High-precision video extensometer based on a simple dual field-of-view telecentric imaging system. measurement 166:108209. https://doi.org/10.1016/j.measurement.2020.108209

Hua T, Xie H, Wang S, Hu Z, Chen P, Zhang Q (2011) Evaluation of the quality of a speckle pattern in the digital image correlation method by mean subset fluctuation. Opt Laser Technol 43(1):9–13

Iraola B, Cabrero J, Basterrechea-Arévalo M, Gracia J (2021) A geometrically defined stiffness contact for finite element models of wood joints. Eng Struct 235:112062. https://doi.org/10.1016/j.engstruct.2021.112062

JAS (2019) JAS1083: Sawn Lumber. Ministry of Agriculture, Forestry and Fisheries

Jeong GY, Park MJ (2016) Evaluate orthotropic properties of wood using digital image correlation. Constr Build Mater 113:864–869. https://doi.org/10.1016/j.conbuildmat.2016.03.129

JIS (2020) JIS Z2101: Methods of test for woods. Minato-ku, Tokyo: Japanese Standards Association

Kang CW, Schwarzkope M, Muszynski L, Jin T, Park HJ, Kang HY, Matsumura J (2014) Mechanical behavior of separated earlywood and latewood of douglas-fir using digital image correlation method. J Fac Agr, Kyushu Univ. https://doi.org/10.5109/1434401

Kumpenza C, Matz P, Halbauer P, Grabner M, Steiner G, Feist F, Müller U (2018) Measuring poisson's ratio: mechanical characterization of spruce wood by means of non-contact optical gauging techniques. Wood Sci Technol 52:1451–1471. https://doi.org/10.1007/s00226-018-1045-7

Li J, Yang G, Siebert T, Shi MF, Yang L (2018) A Method of the direct measurement of the true stress-strain curve over a large strain range using multi-camera digital image correlation. Opt Lasers Eng 107:194–201. https://doi.org/10.1016/j.optlaseng.2018.03.029

Matsuda Y, Fujiwara Y, Murata K, Fujii Y (2017) Residual strain analysis with digital image correlation method for subsurface damage evaluation of Hinoki (Chamaecyparis Obtusa) finished by slow-speed orthogonal cutting. J Wood Sci 63(6):615–624. https://doi.org/10.1007/s10086-017-1659-7

Matsuda Y, Fujiwara Y, Fujii Y (2018) Strain analysis near the cutting edge in orthogonal cutting of Hinoki (Chamaecyparis Obtusa) using a digital image correlation method. J Wood Sci 64(5):566–77

Matsuda Y, Fujiwara Y, Fujii Y (2019) Effect of grain angle on the strain distribution during orthogonal cutting of hinoki (chamaecyparis obtusa) measured using a digital image correlation method. J Wood Sci 65(1):44. https://doi.org/10.1186/s10086-019-1824-2

Murata K, Masuda M (2003) Analysis of strain distribution of softwood in transverse compression measured by digital image correlation method. J Soc Mater Sci Jpn 52(4):347–52

Navaratnam S, Ngo T, Christopher P, Linforth S (2020) The use of digital image correlation for identifying failure characteristics of cross-laminated timber under transverse loading. Measurement 154:107502. https://doi.org/10.1016/j.measurement.2020.107502

Pan B, Asundi A, Xie H, Gao J (2009) Digital image correlation using iterative least squares and pointwise least squares for displacement field and strain field measurements. Opt Lasers Eng 47(7–8):865–874. https://doi.org/10.1016/j.optlaseng.2008.10.014

Pan B, Yu L, Wu D (2013) High-accuracy 2d digital image correlation measurements with bilateral telecentric lenses: error analysis and experimental verification. Exp Mech 53(9):1719–1733. https://doi.org/10.1007/s11340-013-9774-x

Pan B, Yu L, Wu D (2014) High-accuracy 2d digital image correlation measurements using low-cost imaging lenses: implementation of a generalized compensation method. Meas Sci Technol 25(2):025001. https://doi.org/10.1088/0957-0233/25/2/025001

Sirumbal-Zapata LF, Málaga-Chuquitaype C, Elghazouli AY (2019) Experimental assessment and damage modelling of hybrid timber beam-to-steel column connections under cyclic loads. Eng Struct 200:109682. https://doi.org/10.1016/j.engstruct.2019.109682

Teranishi M, Matsubara D (2024) Progressive damage analysis of embedment of metal washer into timber. Wood Mat Sci Eng. https://doi.org/10.1080/17480272.2024.2345191

Timbolmas C, Rescalvo FJ, Portela M, Bravo R (2022) Analysis of poplar timber finger joints by means of digital image correlation (dic) and finite element simulation subjected to tension loading. Eur J Wood Prod 80(3):555–567. https://doi.org/10.1007/s00107-022-01806-6

Totsuka M, Jockwer R, Kawahara H, Aoki K, Inayama M (2022) Experimental study of compressive properties parallel to grain of glulam. J Wood Sci 68(1):33. https://doi.org/10.1186/s10086-022-02040-7

Xavier JC, De Jesus AMP, Morais JJL, Pinto JMT (2012) stereovision measurements on evaluating the modulus of elasticity of wood by compression tests parallel to the grain. Constr Build Mater 26(1):207–215. https://doi.org/10.1016/j.conbuildmat.2011.06.012

Younis N, Kang B (2011) averaging effects of a strain gage. J Mech Sci Technol 25:163–169. https://doi.org/10.1007/s12206-010-1020-1

Authors and Affiliations

Masaki Teranishi[1] · Doppo Matsubara[2]

✉ Masaki Teranishi
mteranishi.10203040@gmail.com

Doppo Matsubara
ft2661@go.tuat.ac.jp

[1] Institute of Science and Technology, Niigata University, 8050, Ikarashi 2-No-Cho, Nishi-Ku, Niigata 950-2181, Japan

[2] Institute of Agriculture, Tokyo University of Agriculture and Technology, 3-8-1, Harumichō, Fuchu-Shi, Tokyo 183-8538, Japan